

# PHENOLOGY CURVE ESTIMATION VIA A MIXED MODEL REPRESENTATION OF FUNCTIONAL PRINCIPAL COMPONENTS: CHARACTERIZING TIME SERIES OF SATELLITE-DERIVED VEGETATION INDICES

INDER TECUAPETLA-GÓMEZ<sup>(1,2)</sup>, FRANCISCO ROSALES-MARTICORENA<sup>(3)</sup>,  
AND BERENICE FANNY GALICIA-GÓMEZ<sup>(4)</sup>

**ABSTRACT.** Vegetation phenology consists of studying synchronous stationary events, such as the vegetation green up and leaves senescence, that can be construed as adaptive responses to climatic constraints. In this paper, we propose a method to estimate the annual phenology curve from multi-annual observations of time series of vegetation indices derived from satellite images. We fitted the classical harmonic regression model to annual-based time series in order to construe the original data set as realizations of a functional process. Hierarchical clustering was applied to define a nearly homogeneous group of annual (smoothed) time series from which a representative and *idealized* phenology curve was estimated at the pixel level. This curve resulted from fitting a mixed model, based on functional principal components, to the homogeneous group of time series. Leveraging the idealized phenology curve, we employed standard calculus criteria to estimate the following *phenological parameters* (stationary events): green up, start of season, maturity, senescence, end of season and dormancy. By applying the proposed methodology to four different data cubes (time series from 2000 to 2023 of a popular satellite-derived vegetation index) recorded across grasslands, forests, and annual rainfed agricultural zones of a Flora and Fauna Protected Area in northern Mexico, we verified that our approach characterizes properly the phenological cycle in vegetation with nearly periodic dynamics, such as grasslands and agricultural areas. The R package `sephora` was used for all computations in this paper.

## 1. INTRODUCTION

In 1751 the botanist Carolus Linnaeus delineated some techniques for gathering annual plant calendars of leaf opening, blooming, fruiting, and leaf fall. Almost a century later, these concepts were used to coin the term *phenology* by the botanist Charles Morren in 1853, cf. Hopp (1974). In the early 1970s the International Biological Program established a Phenology Committee seeking, among other things, to generate the adequate framework for studying ecosystem's phenology, Lieth (1974). As a result of such efforts, this committee came out with the following definition:

---

<sup>1</sup>PROGRAMA INVESTIGADORAS E INVESTIGADORES POR MÉXICO, NATIONAL COUNCIL FOR HUMANITIES, SCIENCE AND TECHNOLOGY (CONAHCYT), MEXICO CITY, MEXICO

<sup>2</sup>GEOMATICS UNIT, NATIONAL COMMISSION FOR THE KNOWLEDGE AND USE OF BIODIVERSITY (CONABIO), MEXICO CITY, MEXICO

<sup>3</sup>GRADUATE SCHOOL OF BUSINESS, UNIVERSIDAD ESAN, LIMA, PERU

<sup>4</sup>LICENCIATURA EN ACTUARÍA, FACULTAD DE CIENCIAS, UNAM, MEXICO CITY, MEXICO

*E-mail addresses:* itecuapetla@conabio.gob.mx, frosales@esan.edu.pe.

**Definition 1.** Phenology is the study of the timing of recurring biological events, the causes of their timing with regard to biotic and abiotic forces, and the interrelation among phases of the same or different species.

Thus, when considering to use this definition in the context of a terrestrial ecosystem, whose dimension can cover a few to hundreds of hectares, Earth Observations (EO) from satellite sensors emerge like the best reliable and economical source of data for such a purpose. In this work, we focused on estimating some phenological parameters (recurring biological events occurring at certain time) from time series of satellite images.

In the last three decades we have seen a sustained interest on applying different mathematical approaches to better understand remotely-sensed vegetation dynamics (Reed et al. (1994), Sellers et al. (1994), Olsson and Eklundh (1994), Roerink et al. (2000), Jakubauskas et al. (2001), Jonsson and Eklundh (2002), Heumann et al. (2007), Jönsson et al. (2010), Sjöström et al. (2011), Melaas et al. (2013), Reyes-González et al. (2021)). Over these years, a certain level of agreement seems to have been achieved about the pertinence of using the classical harmonic regression model to extract the main interannual characteristics of vegetation dynamics when this is registered with a coarse resolution data, cf. Roy and Yan (2020); this data type will be used in this paper applications.

With the use of harmonic regression or other sounding mathematical techniques, it is possible to obtain a smooth (continuous) version of annual vegetation curves. From these curves is relatively easy to estimate certain phenological parameters (calendar dates at which biological events have occurred) as the critical points of some of their derivatives (Zhang et al. (2003), Klosterman et al. (2014)), and subsequent studies of the interannual dynamics of these parameters can be obtained (Boschetti et al. (2009), Eklundh and Jönsson (2015), Zheng et al. (2016), Zeng et al. (2020)).

Due to the release of time series of EO with mid and high resolution, such as Landsat and Sentinel, some researchers have proposed to combine -the fusion of coarse and mid, coarse and high or mid and high resolution images- these datasets and apply different analytical methods to produce annual vegetation phenology curves (Zeng et al. (2016), Filippa et al. (2016), Baumann et al. (2017), Liao et al. (2019), Zhao et al. (2021), Nietupski et al. (2021), Sisseber et al. (2022)). In this paper, we propose an approach to estimate the annual vegetation curve intrinsic to the long-term dynamics of (pixel-based) time series of NASA's Moderate Resolution Imaging Spectroradiometer (MODIS) images.

MODIS images have been available, free of cost, since February 18, 2000. In particular, the MODIS product MOD13Q1 provides pre-processed images of the Normalized Difference Vegetation Index (NDVI); the latest version (6.1) of this product was released in July 2023. Due to its temporal resolution (16 days), a full-length NDVI MOD13Q1 time series (2000-2023) has 549 observations. At the pixel level, we applied the classical harmonic regression model to the original observations and map them into 24 continuous and periodic functions. Then, we applied a typical functional principal component analysis (FPCA) to this set of functions and used a finite number of these FPCs to represent an idealized NDVI curve; the estimation of this idealized curve is performed via a mixed model.

Functional data analysis (FDA) has emerged as a crucial tool in various real-life applications due to its ability to handle complex, high-dimensional data structures commonly encountered in fields such as biology, economics, engineering, and environmental science (Ramsay and Silverman (2005); Ferraty (2006); Kokoszka and Reimherr (2017)). By treating

data as functions rather than discrete points, FDA allows researchers to capture and analyze intricate patterns and relationships over continuous domains (Ramsay and Silverman (2005)). This approach enables a deeper understanding of dynamic systems and processes, leading to more informed decision-making and improved predictive modeling. For instance, in ecology and environmental science, FDA has been instrumental in analyzing spatiotemporal trends in vegetation dynamics (Ferraty (2006); Kokoszka and Reimherr (2017); Yu (2020)), while in economics, it has facilitated the modeling of time-varying risk factors in financial markets (Bai and Ng (2002); Ramsay and Silverman (2005)). One powerful technique within FDA is functional principal component analysis (FPCA), which extracts dominant modes of variation from functional data, allowing for dimensionality reduction and efficient representation of variability (Ramsay and Silverman (2005); Kokoszka and Reimherr (2017)). Applications of FPCA range from characterizing climate patterns (López-Pintado and Romo (2009)) to analyzing brain imaging data (Tian (2010)), showcasing its versatility and effectiveness in diverse domains. To the best of our knowledge FPCA-based applications to recover the phenology curve from satellite images have not yet been explored.

We construe this idealized NDVI curve as a fair approximation to the vegetation phenology curve intrinsic to a pixel. From this curve, we utilized basic calculus’ criterion to find phenological parameters such as Green up (GU), Start of Season (SoS), Maturity (Mat), Senescence (Sen), End of Season (EoS) and Dormancy (Dor) which provide an appropriate characterization of the (remotely-sensed) vegetation cycle.

This paper is organized as follows. In Section 2 we introduced our methodology as well as a mathematically-oriented definition of the phenological parameters mentioned above, see Table 1. Based on this definition and certain conditions, we established that SoS and EoS are always achieved, see Theorem 1. Also in this section, we considered the simplest phenology curve (based on harmonics) and found GU, SoS, Mat and EoS explicitly, see Proposition 1. Section 3 presents three simulation studies assessing the precision of our methods for estimating phenological dates. In Section 4, we considered the MOD13Q1 v6.1 NDVI time series (2000-2023) corresponding to the Flora and Fauna Protected Area *Cerro Mohinora* located at Chihuahua, Mexico; we applied our methodology to describe the phenological cycle in four different land covers: Grasslands, Douglas Fir forest, Pine-Oak forest and Annual Rainfed Agriculture.

## 2. METHODS AND MAIN RESULTS

In this section we present a procedure to compute phenological parameters from long-term NDVI time series (pixel-based) such as the MOD13Q1 product. Conceptually, we begin by disjoining the time series in annual segments that can be seen as functional samples of an underlying NDVI process; this idea is similar in spirit to a profile analysis. Operatively speaking, we begin by representing the annual time series data as a function by fitting a harmonic regression. We then apply a statistical algorithm -based on FPCA- to extract an annual functional signature from the functional NDVI samples, independent of anomalous annual specific variations. Finally, basic calculus criteria are used to identify phenological dates from the resulting signature.

**2.1. Functional data.** Functional data refers to data observed as functions over a continuous domain. Unlike traditional data, which are typically represented as a set of discrete

measurements, functional data are represented as curves or smooth functions, see e.g., Ramsay and Silverman (1997) Ferraty and Vieu (2006), Kokoszka and Reimherr (2018) among many others. This representation allows for the exploration of the inherent structure and variability within the data, capturing the underlying structure of the functional process. To this end, for each pixel in the data set, we first fit the time series data to a harmonic function. We then build a set of functional samples, and remove outlier functional observations.

2.1.1. *Harmonic functions.* Consider the sequence  $\{z_t\}_{t=1}^L$  of NDVI measurements at a given location, taken at a given time  $t$  within certain year, and a characterization of the form

$$z_t = g(t) + \varepsilon_t, \quad \varepsilon_t = \sigma^2 Z, \quad Z \sim N(0, 1), \quad (1)$$

$$g(t) = \theta_0 + \sum_{j=1}^p \left\{ \alpha_j \sin\left(\frac{2\pi j t}{L}\right) + \beta_j \cos\left(\frac{2\pi j t}{L}\right) \right\}, \quad t = 1, 2, \dots, L, \quad (2)$$

where  $g$  is assumed to be a continuous periodic function, and thus suitable to be approximated by the addition of various sine and cosine functions of varying amplitude ( $\alpha_j, \beta_j$ ), and period ( $2\pi j/L$ ). To the best of our knowledge most of the empirical studies on NDVI time series have considered  $p = 3$  or  $p = 4$ , cf. Eastman et al. (1993).

Model (1) can be written in matrix form as

$$\mathbf{z} = \mathbf{X}\boldsymbol{\beta} + \boldsymbol{\varepsilon}, \quad \boldsymbol{\varepsilon} \sim N(\mathbf{0}, \sigma^2 \mathbf{I}), \quad (3)$$

where  $\mathbf{z}, \boldsymbol{\varepsilon} \in \mathbb{R}^L$ ,  $\boldsymbol{\beta} \in \mathbb{R}^{2p+1}$ , and  $\mathbf{X}$  is the design matrix ( $L \times (2p+1)$ ) of the form

$$\mathbf{X} = \begin{bmatrix} 1 & \sin\left(\frac{2\pi}{L}\right) & \cos\left(\frac{2\pi}{L}\right) & \dots & \sin\left(\frac{2p\pi}{L}\right) & \cos\left(\frac{2p\pi}{L}\right) \\ 1 & \sin\left(\frac{4\pi}{L}\right) & \cos\left(\frac{4\pi}{L}\right) & \dots & \sin\left(\frac{4p\pi}{L}\right) & \cos\left(\frac{4p\pi}{L}\right) \\ \vdots & \vdots & \dots & \vdots & \vdots & \\ 1 & \sin(2\pi) & \cos(2\pi) & \dots & \sin(2p\pi) & \cos(2p\pi) \end{bmatrix}. \quad (4)$$

Estimation of (3) requires identification of parameter vector  $\boldsymbol{\vartheta} = \{\theta_0, \alpha_1, \dots, \alpha_p, \beta_1, \dots, \beta_p, \sigma\}$ , and selection of hiper-parameter  $p$ . Model (3) is applied to each set of annual observations; for our application, we ended up with 24 smoothed NDVI annual functions.

2.1.2. *Hierarchical clustering.* We apply hierarchical clustering, cf. Everitt et al. (2011), to the set of NDVI smoothed functions obtained in the previous section. We utilize the function `tsclust` of the R package `dtwclust` by Sardá-Espinosa (2023) as the main engine to perform clustering. We set `tsclust` to find two clusters only. By doing so, we aim to find a subset of functions which are similar -close in distance- and at the same time discard from the functional dataset those curves with an atypical behavior. Although this step intends to facilitate the application of the upcoming FPCA algorithm, by pre-selecting a set of highly similar curves, our implementation also allows for the use of either of the two clusters or the entire functional dataset in the FPCA step.

2.2. **Functional principal components.** A random variable  $\mathcal{F}$  is called a functional variable if it takes values in an infinite dimensional space (or functional space). Since  $\mathcal{F}$  is a random curve, we can identify it as  $\mathcal{F} = \{\mathcal{F}(t); t \in [0, 1]\}$ . Functional data analysis (FDA) takes place in a functional data set  $f_1, \dots, f_m$  of realizations of  $m$  functional variables  $\mathcal{F}_1, \dots, \mathcal{F}_m$ , identically distributed as  $\mathcal{F}$ , where an observation  $f$  of  $\mathcal{F}$  is called “functional data”. We highlight that we assume the functional observations  $f_1, \dots, f_m$  are independent.

The interested reader is referred to Kokoszka and Reimherr (2018) to explore the dependence case.

Our functional data is given as a collection of functions sampled at  $n$  equidistant points and arranged as a rectangular matrix with  $m$  columns and  $n$  rows. Let  $\mathbf{Y} = (\hat{\mathbf{z}}_1^\top, \hat{\mathbf{z}}_2^\top, \dots, \hat{\mathbf{z}}_m^\top)^\top$ , where each functional observation is captured in the columns of  $\mathbf{Y}$  and corresponds to the estimation of different samples of NDVI at the same location for different years using model (1)-(3). The goal of FPCA is to identify the functional principal components that explain most of the variance in matrix  $\mathbf{Y}$ , and use them to build an overall trend curve  $\tau$ , that represents the NDVI signature at a given location, regardless of the year. In this subsection we present the general theory of FPCA and the corresponding estimation algorithm.

*2.2.1. Principal components.* Consider function  $f_j(t)$  for  $j = 1, 2, \dots, m$ , defined in the compact interval  $[0, 1]$  as functional data. More specifically, assume each  $f_j(t)$  is an independent realisation of the stochastic process  $\{f(t), t \in [0, 1]\}$  with mean  $\mathbb{E}[f(t)] = \tau(t)$  and covariance kernel  $\mathcal{K}(x, z) = \text{cov}\{f(t), f(z)\}$ ,  $x, z \in [0, 1]$ . Mercer's lemma states that if  $\int_0^1 \mathcal{K}(x, x) dx < \infty$  then there exists an orthonormal sequence of eigenfunctions  $\{\zeta_j\}_{j=1}^\infty$  and non-increasing, non-negative sequence of eigenvalues  $\{\kappa_j\}_{j=1}^\infty$  such that for  $(\mathcal{K}\zeta_j)(t) := \int_0^1 \mathcal{K}(x, z)\zeta_j(z)dz = \kappa_j\zeta_j(t)$ , it holds that

$$\mathcal{K}(x, z) = \sum_{j=1}^{\infty} \kappa_j \zeta_j(x) \zeta_j(z), \text{ and } \sum_{j=1}^{\infty} \kappa_j = \int_0^1 \mathcal{K}(x, x) dx.$$

Hence we can write the Karhunen-Loève expansion as

$$f(t) = \tau(t) + \sum_{j=1}^{\infty} \sqrt{\kappa_j} \xi_j \zeta_j(t), \quad (5)$$

where  $\xi_j := \frac{1}{\sqrt{\kappa_j}} \int f(t)\zeta_j(z)dz$ ,  $\mathbb{E}[\xi_j] = 0$ ,  $\mathbb{E}[\xi_j, \xi_k] = \delta_{jk}$ ,  $j, k \in \mathbb{N}$  and  $\delta_{jk}$  is the Kronecker delta. From (5) the implementation of a reduced rank model for a sample  $j = 1, 2, \dots, m$  as presented in e.g. James et al. (2000) can be written as

$$f_j(t) = \tau(t) + \sum_{k=1}^h \psi_k(t) v_{jk} = \tau(t) + \mathbf{\Psi}(t)^\top \mathbf{v}_j \quad (6)$$

where  $h$  is a finite integer usually  $h \ll m$ ,  $\mathbf{\Psi}(t) = \{\psi_1(t), \psi_2(t), \dots, \psi_h(t)\}^\top$  contain the  $k$ -th principal component (PC) function  $\psi_k(t)$  and  $\mathbf{v}_j = \{v_{j1}, v_{j2}, \dots, v_{jh}\}^\top$  is the vector of PC scores for the  $j$ -th curve. Moreover, we can interpret each  $f_j(t)$  in (6) as a curve composed by an overall trend  $\tau(t)$  and a subject specific deviation  $\eta_j(t) := \sum_{k=1}^h \psi_k(t) v_{jk}$ .

Thus, given observation pairs  $(t_i, y_{i,j})$  for  $i = 1, \dots, L$  and  $j = 1, \dots, m$ , one can write an additive model of the form

$$y_{i,j} = \tau(t_i) + \eta_j(t_i) + \epsilon_{i,j}, \quad (7)$$

where  $\tau(t)$  is an unknown smooth function and  $\{\epsilon_{i,j}\}_{i=1}^n$  is the uncorrelated homoscedastic error measurement of curve  $j$ , i.e.  $\text{Cor}(\epsilon_{i,j}, \epsilon_{k,j}) = \mathbb{1}_{\{i=k\}}$  for any  $(i, j)$  pair. Given a unique smoothness class  $q = 2$  for all curves, see Krivobokova et al. (2022) for details, we can represent the unknown functions as  $\tau(t) = \mathbf{C}_\tau(t)\boldsymbol{\theta}_\tau$  and  $\psi_j(t) = \mathbf{C}_\psi(t)\boldsymbol{\theta}_{\psi_j}$ . For the last case

we can also write  $\Psi(t)^\top = \mathbf{C}_\psi(t)\Theta_\psi$  with  $\Theta_\psi = \{\boldsymbol{\theta}_{\psi_1}, \dots, \boldsymbol{\theta}_{\psi_h}\}$  an  $n \times h$  matrix such that

$$\int \Psi(t)\Psi(t)^\top dx = \Theta_\psi^\top \left( \int \mathbf{C}(t)^\top \mathbf{C}(t) dx \right) \Theta_\psi = \mathbf{I}_h,$$

holds, and the usual orthogonality requirements for the principal component curves are satisfied. It follows that  $\Theta_\psi^\top \Theta_\psi = \mathbf{I}_h$  and thus the estimation problem in (6) is reduced to the computation of the spline coefficients  $\boldsymbol{\theta}_\tau, \boldsymbol{\theta}_{\psi_k}$  for  $j = 1, \dots, m$ , and  $k = 1, \dots, h$  in

$$\begin{aligned} \min_{\boldsymbol{\theta}_\tau, \boldsymbol{\theta}_{\psi_k}} & \left[ \frac{1}{n} \sum_{j=1}^m (\mathbf{y}_j - \mathbf{C}_\tau \boldsymbol{\theta}_\tau - \mathbf{C}_\psi \Theta_\psi v_j)^\top (\mathbf{y}_j - \mathbf{C}_\tau \boldsymbol{\theta}_\tau - \mathbf{C}_\psi \Theta_\psi v_j) \right. \\ & + \lambda_\tau \boldsymbol{\theta}_\tau^\top \left( \int_0^1 \{\mathbf{C}_\tau(t)^{(2)}\}^\top \{\mathbf{C}_\tau(t)^{(2)}\} dt \right) \boldsymbol{\theta}_\tau \\ & \left. + \lambda_\psi \sum_{k=1}^h \boldsymbol{\theta}_{\psi_k}^\top \left( \int_0^1 \{\mathbf{C}_\psi(t)^{(2)}\}^\top \{\mathbf{C}_\psi(t)^{(2)}\} dt \right) \boldsymbol{\theta}_{\psi_k} \right], \end{aligned} \quad (8)$$

where  $\mathbf{v}_j$  is a random vector such that  $\mathbf{v}_j \sim \mathcal{N}(\mathbf{0}, \sigma_{v_j} \mathbf{I}_m)$ , we denote  $\Psi = \mathbf{C}_\psi \Theta_\psi$  and  $\Theta^\top \Theta = \mathbf{I}_h$ . Given  $h$  it remains to estimate  $\mathbf{v}_j, \lambda_\tau$  and  $\lambda_\psi$  for which one can utilize the mixed models representation of penalized splines, see e.g. Ruppert and Carroll (2003). The estimation of the full additive model as in (7) it is implemented as part of the function `phenopar` of our R package `sephora`.

**2.2.2. Statistical algorithm.** Here we present the two main steps of the statistical algorithm implemented to identify  $\tau(t)$  in (7).

Step 1:

1. Solve (8) for a trend only model, i.e. for  $\mathbf{C}_\psi \Theta_\psi v_j = 0$  for all  $j$ , to obtain  $\lambda_\tau$  and compute

$$\hat{\boldsymbol{\theta}}_\tau^{(0)} = (\mathcal{C}_\tau^\top \mathcal{C}_\tau + \lambda_\tau n \mathcal{D}_\tau)^{-1} \mathcal{C}_\tau^\top \mathbf{Y} \quad (9)$$

with  $\mathcal{C}_\tau = \mathbf{C}_\tau \otimes \mathbf{I}_m$  and  $\mathcal{D}_\tau = \mathbf{D}_\tau \otimes \mathbf{I}_m$ .

2. Write the residuals for each curve as  $\mathbf{r}_j = \mathbf{y}_j - \mathbf{C}_\tau \hat{\boldsymbol{\theta}}_\tau^{(0)}$  and fit the linear least squares model

$$\mathbf{r}_j = \mathbf{C}_\psi \boldsymbol{\Gamma}_j + \boldsymbol{\epsilon}_j,$$

to obtain  $\hat{\boldsymbol{\Gamma}}^{(0)} = (\hat{\boldsymbol{\Gamma}}_1^{(0)}, \dots, \hat{\boldsymbol{\Gamma}}_m^{(0)})^\top$ .

3. Calculate the singular value decomposition

$$\hat{\boldsymbol{\Gamma}}^{(0)} = \mathbf{U} \boldsymbol{\Sigma} \mathbf{V}^\top,$$

and set  $\hat{\boldsymbol{\theta}}_{\psi_k}^{(0)} = \mathbf{V}_k \boldsymbol{\Sigma}_k$ , and hence  $\hat{\Psi}^{(0)} = \mathbf{C}_\psi \hat{\Theta}_\psi^{(0)}$ .

Step 2:

Given  $h$ , initial value  $\hat{\Psi}^{(0)}$  and parametrisation  $\Phi$ , update the computation of  $\hat{\boldsymbol{v}}^{(l)}$  in (8) for the  $l$ -th iteration and the corresponding  $\hat{\Psi}^{(l)}$  matrix until convergence is achieved.

1. Solve (8) given  $\hat{\Theta}_\psi^{(l-1)}$  and update  $\hat{\mathbf{v}}^{(l)}$  and  $\hat{\lambda}_\tau^{(l)}$  to compute

$$\hat{\boldsymbol{\theta}}_\tau^{(l)} = \left\{ \mathbf{C}_\tau^\top \mathbf{C}_\tau + \hat{\lambda}_\tau^{(l)} n \mathbf{D}_\tau \right\}^{-1} \mathbf{C}_\tau^\top \mathbf{Y},$$

with  $\mathbf{C}_\tau$  and  $\mathbf{D}_\tau$  as defined on the initialisation step.

2. Write the residuals as  $\mathbf{r}^{(l)} = \mathbf{Y} - \mathbf{C}_\tau \hat{\boldsymbol{\theta}}_\tau^{(l)}$  and fit the penalised least squares model

$$\mathbf{r}^{(l)} = \mathbf{C}_\psi \hat{\Theta}_\psi^{(l-1)} \hat{\mathbf{v}}^{(l)} + \boldsymbol{\epsilon},$$

to update  $\hat{\Theta}_\psi^{(l)}$  by

$$\hat{\boldsymbol{\theta}}_{\psi_k}^{(l)} = \left\{ \sum_{j=1}^N \left( \hat{v}_{jk}^{(l)} \right)^2 \mathbf{C}_\psi^\top \mathbf{C}_\psi + \hat{\lambda}_\psi^{(l)} \mathbf{D}_\psi \right\}^{-1} \left\{ \sum_{j=1}^N \left( \hat{v}_{jk}^{(l)} \right) \mathbf{C}_\psi^\top \left( \mathbf{Y}_j - \mathbf{C}_\tau \hat{\boldsymbol{\theta}}_\tau^{(l)} - \mathbf{C}_\psi \hat{\mathbf{Q}}_{jk}^{(l)} \right) \right\},$$

for

$$\hat{\mathbf{Q}}_{jk}^{(l)} = \sum_{l \neq k} \hat{\boldsymbol{\theta}}_{\psi_l}^{(l)} \hat{v}_{jl}^{(l)}, \quad j = 1, \dots, N.$$

3. Construct  $\hat{\Theta}_\psi^{(l)}$  and use the QR decomposition to orthonormalise its columns. With the new estimation of  $\hat{\Theta}_\psi^{(l)}$  go back to step one until convergence is achieved.

**2.3. Phenological date estimation.** We propose a formal definition of phenological date estimates which is based on the second derivative criterion from basic calculus. Let  $\tau : \mathcal{D} \rightarrow \mathbb{R}$  denote the idealized NDVI signature obtained via FPCA. Table 1 shows our definition in an schematic manner. Our definition, involves the first four derivatives of  $\tau(x)$ ,  $x \in \mathcal{D}$ , and we believe that complements the treatment of phenological dates presented in Baumann et al. (2017).

TABLE 1. Definition of phenological parameters

Phenological parameter	Notation	Critical point	$\tau^{(2)}$	$\tau^{(3)}$	$\tau^{(4)}$
Green up	$x_{GU}$	$\tau^{(2)}$ (global) maximum	.	0	-
Start of season	$x_{SoS}$	$\tau^{(1)}$ (global) maximum	0	-	.
Maturity	$x_{Mat}$	$\tau^{(2)}$ (global) minimum	.	0	+
Senescence	$x_{Sen}$	$\tau^{(2)}$ (local) minimum	.	0	+
End of season	$x_{EoS}$	$\tau^{(1)}$ (global) minimum	0	+	.
Dormancy	$x_{Dor}$	$\tau^{(2)}$ (local) maximum	.	0	-

In addition to Table 1's definition, the general -and natural- constraint must be imposed:

$$x_{GU} < x_{SoS} < x_{Mat} < x_{Sen} < x_{EoS} < x_{Sen} < x_{Dor}. \quad (10)$$

Thus, it is immediate that

**Theorem 1.** *Suppose that  $\tau$  is the mean trend function of the additive model (7). Then, the phenological parameters Start and End of season always exist on the interval  $[0, L]$ . Also, either Green up or Dormancy and Maturity or Senescence always exist on the interval  $[0, L]$ .*

**Proof.** The existence of Start and End of Season is ensured by the continuity of  $\tau^{(1)}$  on  $[0, L]$ . Similarly, the continuity of  $\tau^{(2)}$  on  $[0, L]$  ensures that either Green up or Dormancy (and Maturity or Senescence) exist.  $\square$

One limitation of our method is that the precision of the estimation of  $\tau^{(\nu)}$  decreases in  $\nu$ , thus the estimation of Start and End of season, which only require the estimation of the second and third derivative of  $\tau$ , is expected to be more precise than that of any other phenological date.

In order to provide a better understanding of the limitations of our method, we consider the case of estimating the phenological parameters on the simplest of harmonic functions: the cosine function.

**Proposition 1.** *Let  $\tau$  be the mean trend function of the additive model (7). Suppose further that  $\tau$  follows the representation*

$$\tau(t) = c_0 + c_1 \cos\left(\frac{2\pi t}{L} - \varphi_1\right), \quad (11)$$

where  $c_0, c_1 \in \mathbb{R}^+$  and  $\varphi_1 \in (0, 360)$ . Then

$$\begin{aligned} x_{GU} &= \frac{(\varphi_1 - 180)L}{360} \mathbb{1}_{[180, \infty)}(\varphi_1) \\ x_{SoS} &= \frac{(\varphi_1 - 90)L}{360} \mathbb{1}_{[90, \infty)}(\varphi_1) \\ x_{Mat} &= x_{Sen} = \frac{L}{360} \varphi_1 \\ x_{EoS} &= \frac{(\varphi_1 + 90)L}{360} \mathbb{1}_{[0, 270)}(\varphi_1) \\ x_{Dorm} &= \frac{(\varphi_1 + 180)}{360} \mathbb{1}_{[0, 180)}(\varphi_1). \end{aligned}$$

**Remark 1.** We have set  $x_{Sen}$  equal to  $x_{Mat}$  because  $\tau^{(2)}$  has only one minimum on  $[0, L]$ . In order for  $x_{SoS}$  and  $x_{EoS}$  to be found on the interval  $[0, L]$ , it is necessary that  $90 \leq \varphi_1 < 270$ . Observe also that if  $\varphi_1 \in [180, 270)$ , then  $x_{GU}$  is well-defined on the interval  $[0, L]$  but, in this case,  $x_{Dor}$  cannot be found on the same interval. Similarly, if  $\varphi_1 \in [90, 180)$ , then  $x_{Dor}$  is found on the interval  $[0, L]$  at the expense of not being able to find  $x_{GU}$ .

According to this proposition, the estimates of phenological parameters are in correspondence with the phase angle  $\varphi_1$ . Also, from the remark it follows that with a single harmonics, is possible to estimate 4 phenological parameters at most:  $x_{GU}$ ,  $x_{SoS}$ ,  $x_{Mat} = x_{Sen}$  and  $x_{EoS}$  if  $\varphi \in \varphi_1 \in [180, 270)$ ; and  $x_{SoS}$ ,  $x_{Mat} = x_{Sen}$ ,  $x_{EoS}$  and  $x_{Dor}$  if  $\varphi \in \varphi_1 \in [90, 180)$ .

### 3. SIMULATIONS

In this section we present a set of simulation studies aiming to assess the precision of our methodology for estimating the so-called phenological parameters as they are defined in Table 1.

**3.1. sephora: Well-implemented routines.** We begin this section by providing evidence that the routines that will be employed in the upcoming simulation studies have been implemented correctly. To this end, we consider the signal described in Eq. (11) with  $c_0 = 0$ ,  $c_1 = 1$ ,  $L = 23$ ,  $\varphi = 210$  and  $t \in (0, 23)$ . We produced 23 observations from this curve. Then, we fitted the corresponding harmonic regression model (via the function `haRmonics` of the R package `geoTS` by Tecuapetla-Gómez (2022)) to these observations; this allows us to get a numerical function from which (and its derivatives) we can get critical points (phenological parameters). Next, we applied the functions `ndvi_derivatives` (to get the first fourth derivatives of the numerical function just mentioned), `global_min_max` (to get green-up, start of season, maturity and end of season) and `local_min_max` (to get senescence) of the R package `sephora`. Finally, we obtained the results showed in the Table 2.

TABLE 2. Comparison of theoretical phenological parameters as provided by Proposition 1 and the estimates given by the R package `sephora`.

Phenological parameters	Theoretical solutions	<code>sephora</code> estimates
GU	1.916667	1.916667
SoS	7.666667	7.666667
Mat	13.416667	13.416667
EoS	19.166667	19.166667

In what follows, we will show results based on the use of `sephora`'s `phenopar` function. This function depends internally on `haRmonics`, `ndvi_derivatives`, `global_min_max` and `local_min_max`, among many other functions. In addition to the beginning and end of the time series, `phenopar` requires the arguments: `numFreq` (the number of frequencies employed by `haRmonics` in the smoothing step), `distance` (the functional distance employed in the hierarchical clustering step), `k` (the number of functional principal components), `basis` and `samples` (these 2 arguments are used to calculate the Demmler-Reinsch basis numerically, the length of each member of the basis is equal to `samples`).

Unless specified otherwise, we used `numFreq=1`, `k=1`, `samples=50` and since we are interested in measuring the robustness of our methodology to the distance used in the hierarchical clustering step, for each simulated time series, the phenological parameters were estimated under `distance=dtw_basic` and `distance=dtw2`.

**3.2. Homoscedastic error noise.** In order to assess the performance of our methodology on time series whose length is comparable with that of our applications' time series, we replicated the base signal described in the previous section (with the same parameters) 23 times; we ended up with a signal with 552 observations. To this signal we added randomly generated numbers distributed Gaussian with zero mean and standard deviation  $\sigma \in \{0.125, 0.25, 0.5\}$ . We repeated this procedure 1000 times. In order to assess our results we employed the mean squared error (MSE) of the estimates produced by `sephora`. The results of this simulation study are summarized in the Table 3 (in its first 6 rows).

**3.3. Heteroscedastic error noise.** Some investigations suggest that the variability of an NDVI time series depends on the date at which every image has been acquired, Borgogno-Mondino et al. (2016). In order to assess the performance of our procedure in this context, we employed the signal described in the previous section but now we perturbed it as follows. First, we added a seasonally dependent trend to each of the 23 seasons within the base signal.

TABLE 3. The MSE of phenological parameter estimates (as provided by `phenopar`) under iid error noise, based on 1000 pseudo samples each of size 552. Base signal is described in the Section 3.1.

$\sigma$	$df$	Distance	GU	SoS	Mat	EoS
0.15		Basic	0.0834128	0.1129451	0.1026047	0.0927606
0.15		L2	0.0834128	0.1129451	0.1026047	0.0927606
0.25		Basic	0.0834128	0.1129451	0.1026047	0.0927606
0.25		L2	0.0834128	0.1129451	0.1026047	0.0927606
0.5		Basic	0.1237819	0.1129451	0.1026047	0.0927606
0.5		L2	0.1237819	0.1129451	0.1469444	0.1351150
	1	Basic	0.0833804	0.0745310	0.0662063	0.0927262
	1	L2	0.0833804	0.0745310	0.0662063	0.0927262

To be more precise, to each season, we summed up a randomly generated number distributed Gaussian with zero mean and standard deviation 0.7229 (this is the standard deviation of the 23 observations introduced in Section 3.1) to each observation within a season. Next, we added a heavy-tailed heteroscedastic noise as follows. We produced 23 randomly generated numbers distributed  $\chi^2$  with  $df$  degrees of freedom, the first element of this set of numbers is added to the first observation within each season, the second element is added to each season's second observation and so on. The MSE of 1000 simulations of the procedure just described are shown in the Table 3 (in its last 2 rows).

TABLE 4. The MSE of phenological parameter estimates (as provided by `phenopar`) under heteroscedastic error noise, based on 1000 pseudo samples each of size 552. Base signal is described in the Section 3.1.

numFreq	$\sigma$	$df$	Distance	GU	SoS	Mat	EoS	
2	0.15		Basic	0.0099451	0.0533524	1.157987	0.5555487	
	0.15		L2	0.0099451	0.0533524	1.157987	0.5555487	
	0.25		Basic	0.0013511	0.1275044	2.303049	0.7598426	
	0.25		L2	0.0013511	0.1275044	2.303049	0.7598426	
	0.5		Basic	0.0231901	0.4517804	5.758904	0.9954390	
	0.5		L2	0.0231901	0.4517804	5.758904	0.9954390	
		1	Basic	0.0774567	0.0282363	1.936418	0.3098269	
		1	L2	0.0774567	0.0282363	1.936418	0.3098269	
	3	0.15		Basic	0.7147583	0.2757449	1.136317	1.5619293
		0.15		L2	1.2044812	0.3458944	1.420886	0.8736701
0.25			Basic	1.9953175	0.7059069	2.465187	1.2628012	
0.25			L2	2.5651167	0.3458944	3.094547	0.7598426	
0.5			Basic	2.9846901	0.6039916	4.044874	1.2628012	
0.5			L2	433.9421656	0.4239853	12.938639	0.3839472	
		1	Basic	2.565117	0.1592702	3.79538	4.910575	
		1	L2	2.565117	0.1592702	3.79538	4.910575	

**3.4. Misspecified model.** In the previous studies, we assumed that the model was correctly specified, that is, we used the correct number of frequencies (`numFreq=1`) in the harmonic regression model that estimates the one-frequency base signal introduced in Section 3.1. In this study, we considered the setups described in the previous two studies, but used

`numFreq=2` and `numFreq=3` in the estimation process. For the case of homoscedastic errors, when `numFreq=3` and  $\sigma < 0.5$  we had to use a `basis` built with `samples=75` for the algorithm described in Section 2.2.2 to converge. When  $\sigma = 0.5$  it was necessary to utilize  $k = 2$  for the estimation algorithm to converge. Table 4 summarizes the results of this study.

#### 4. APPLICATIONS

In this section we apply our methodology to MOD13Q1 NDVI time series from pixels located at the grasslands, Douglas Fir forest, Pine-Oak forest and annual rainfed agriculture at the Flora and Fauna Protected Area Cerro Mohinora; see Figure 1. These four cover lands were generated by INEGI in its latest national land use cartography.

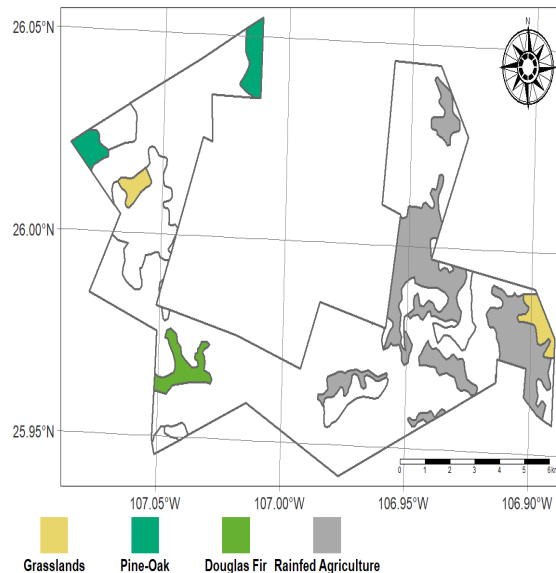


FIGURE 1. Flora and Fauna Protected Area Cerro Mohinora at Chihuahua, Mexico.

**4.1. Working at the pixel level.** In Figure 2 we show annual, smoothed, re-sampled and overlapped NDVI time series from some pixels located at the four cover lands shown in Figure 1. We will call *profile plot* to this type of plot. For smoothing we applied a harmonic regression model with three frequencies to each of the original, annual NDVI time series. Resampling was employed to enhance the interpretation of the estimated phenological dates which, naturally, occur at some days along a solar year.

Typically, grasslands and rainfed agricultural areas show a quick reaction to changes in the climatic conditions. For instance, in grasslands it is expected to observe small NDVI values ( $< 0.4$ ) throughout the dry season. This characteristic starts to change even right after the first rain of the season, starting from which we can expect a steady sequence of increments in NDVI values until the maturity of the vegetation is reached. Having overpassed maturity, it is expected to observe a decreasing behavior in NDVI curves. Thus, NDVI time series from pixels located at these land covers are expected to exhibit a distinctive periodic behavior, see panels A and D in Figure 2.

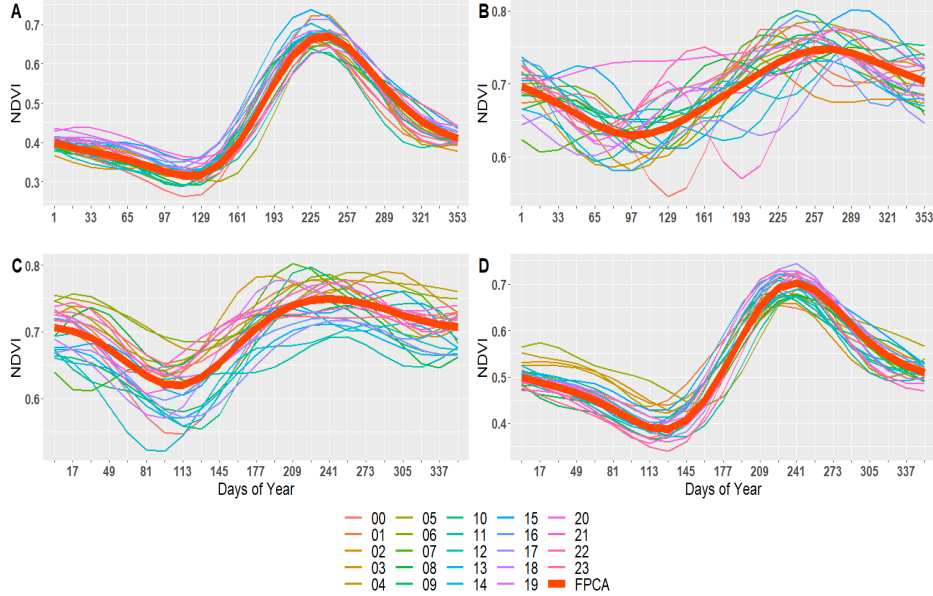


FIGURE 2. NDVI profile plots with idealized NDVI taken from: (A) Grasslands, (B) Douglas Fir forest, (C) Pine-Oak forest and (D) Annual rainfed agriculture.

Unlike grasslands and agricultural areas, NDVI recorded at forests tend to show a less clear periodic annual behavior. In panels B and C of Figure 2 we include profile plots of pixels located at the Douglas Fir and Pine-Oak forests of Cerro Mohinora. As shown in these figures, throughout the year, NDVI values are rather high, (for both sets of time series, the median and standard deviation are close to 0.7 and 0.05, respectively), in contrast with NDVI values registered at grasslands (the set of time series of panel A has median 0.41 and s.d. 0.11) and agricultural areas (the set of time series of panel D has median 0.51 and s.d. 0.10).

We applied a hierarchical clustering to each of the four groups of smoothed and re-sampled NDVI time series of Figure 2. We used the basic dynamic time warping distance provided by package X in each case; although similar results were obtained with other distances. We only allowed for the creation of two clusters. For the pixel shown in panel A the smaller cluster was comprised by the years 2015, 2016, 2017, 2019 and 2020 allocating the remaining 19 years to the larger cluster. We found a similar behavior in the pixel of the panel D, the smaller cluster was formed by the years 2001-2005, though. For the pixel of the panel B, located at the Douglas Fir forest, hierarchical clustering suggested to discard the year 2020 leaving the dominating cluster with 23 years. Finally, for the pixel in the panel C the resulting clusters have sizes 13 and 11.

In addition to the profile plots, Figure 2’s panels include the *idealized* NDVI (thick, red line) produced by our methodology. Each idealized NDVI is the estimated trend curve of model (X) based on the smoothed, re-sampled NDVI curves in the *dominating* cluster obtained via the aforementioned hierarchical clustering. We defined a dominating cluster as that cluster with at least 15 curves -which represents slightly more than the 60% of the total amount of curves in each group. Hence, in Figure 2 the only group without a dominating

	DoY	Date	DoY	Date	DoY	Date	DoY	Date
GU	144	May 24	97	April 7	109	April 19	144	May 24
SoS	183	July 2	184	July 3	157	June 6	185	July 4
Mat	228	Au. 16	262	Sep. 19	31	Jan. 31	229	Au. 17
Sen	66	March 7	20	Jan. 20	196	July 15	63	March 4
EoS	280	Oc. 7	46	Feb. 15	63	March 4	282	Oc. 9
Dor	312	No. 8	333	No. 29	329	No. 25	313	No. 9

TABLE 5. Estimated phenological dates (in days of the year, DoY, and regular dates) for the pixels shown in Figure 3.

group is that in panel C, in this case we opted for estimating the idealized NDVI based on the entire 24 annual time series.

Table 5 shows the estimates of the phenological parameters, green up (GU), start of season (SoS), maturity (Mat), senescence (Sen), end of season (EoS) and dormancy (Dor) for each of the four groups of time series discussed so far. These estimates are the critical points, see Eq. (W), of the idealized NDVI curve of each time series set.

There exists an evident similarity in the estimated phenological cycles of grasslands and rainfed agricultural pixels. In both cases, the green up occurs at the same date, their seasons start and end within a difference of two days, there is a difference of one day in their corresponding maturity and dormancy points. When studying vegetation’s dynamics, it is relevant to know the length of the season, that is, the difference between the end and start of the season dates. Based on our procedure, the season’s length is 97 days for the pixels shown in panels A and D of Figure 2.

Based on Table 5, our procedure is able to estimate at least three out of the six phenological parameters that comprise the entire cycle for NDVI recorded at forests. Indeed, for the Douglas Fir forest pixel, the estimated dates for green up, start of season, maturity and dormancy follow a sensible chronological order. For the Pine-Oak forest pixel, whose dynamics seems to be more intricate, our approach produces meaningful estimates for green up, start of season and dormancy.

Unfortunately, the senescence’s estimate produced by our approach does not seem to be realistic.

**4.2. Working at the polygon level.** The analysis shown in the previous section provides evidence that our approach to estimate the phenological cycle will produce better results on land covers with a vegetation exhibiting a clear periodic dynamics such as grasslands and annual rainfed agricultural zones. In this section we present the results of applying our approach to all the pixels of each of the polygons shown in Figure 1.

The grasslands, Douglas Fir forest, Pine-Oak forest and annual rainfed agriculture polygons contain 62, 56, 72 and 441 pixels, respectively. The time series of each pixel of these polygons were analyzed utilizing the same specifications discussed in the previous section. Computation was efficiently carried out through parallel computing via the `phenopar_polygon` function of our R package `sephora`.

After disregarding outliers and estimates lying outside an empirical 95% confidence interval (based on median and median absolute deviation), Figure 3 shows Archimedean spirals plots

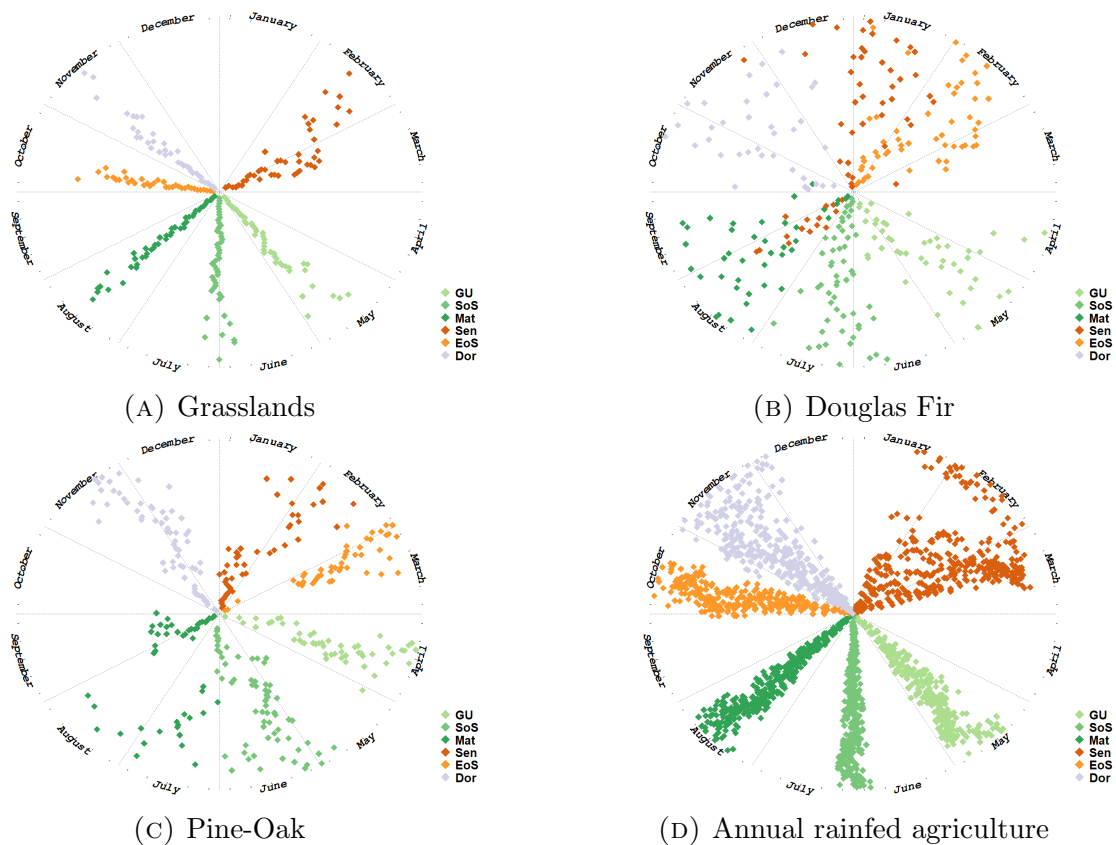


FIGURE 3. Spiral plots of estimated phenological parameters for all the pixel in each of the polygons shown in Figure 2.

displaying the estimated phenological parameters from each pixel in loops around the interval  $[0, 2\pi]$ ; a loop is completed once the six parameters of a single pixel are drawn in the plot.

Outliers removal varied between parameters and polygons. For grasslands, start of season (12%) and end of season (37%) suffered from a minimal and maximal outlier removal. In the star of season, maturity, senescence and dormancy estimates over the Douglas Fir forest there were no outlier found and the maximum outlier removal was observed in green up (5.35%). In the star of season, maturity, senescence and end of season estimates over the Pine-Oak forest there were no outlier found and the maximum outlier removal was observed in green up (15.27%). Finally, for the Annual rainfed agriculture pixels, senescence (3.4%) and end of season (24.7%) experienced a minimal and maximal outlier removal.

The main objective of this study is to characterize vegetation’s phenological cycle based on information registered in pixels from well-defined polygons. Thus, Table 6 summarizes the median and median absolute deviation (in regular dates) of each phenological parameter estimates distribution obtained from the pixels in the polygons of Cerro Mohinora. As argued above, disregarding the senescence date, our approach produces sensible results about the phenological cycle in vegetations with pseudo-periodic seasons such as grasslands and annual rainfed agriculture.

	Grasslands	Douglas Fir	Pine-Oak	Agriculture
GU	May 24 ( $\pm 3$ days)	May 21 ( $\pm 16$ days)	April 20 ( $\pm 7$ days)	May 23 ( $\pm 4$ days)
SoS	July 2 ( $\pm 3$ days)	July 11 ( $\pm 9$ days)	June 10 ( $\pm 13$ days)	July 2 ( $\pm 3$ days)
Mat	Au. 17 ( $\pm 1$ days)	Au. 25 ( $\pm 13$ days)	Au. 27 ( $\pm 24$ days)	Au. 17 ( $\pm 4$ days)
Sen	March 4 ( $\pm 13$ days)	Au. 7 ( $\pm 215$ days)	Jan. 24 ( $\pm 15$ days)	March 2 ( $\pm 19$ days)
EoS	Oc. 9 ( $\pm 1$ days)	Feb. 11 ( $\pm 19$ days)	March 7 ( $\pm 5$ days)	Oc. 11 ( $\pm 6$ days)
Dor	No. 12 ( $\pm 3$ days)	Oc. 29 ( $\pm 19$ days)	No. 26 ( $\pm 9$ days)	No. 14 ( $\pm 10$ days)

TABLE 6. Median and median absolute deviation of estimated phenological dates for the polygons shown in Figure 2.

## 5. ACKNOWLEDGMENTS

We are grateful to Lizbeth Naranjo-Albarrán and Ruth Fuentes-García with Facultad de Ciencias at Universidad Nacional Autónoma de México for helpful discussions that contributed to improve this work. This paper also benefited from discussions with Leticia Ramírez at CIMAT, Guanajuato. Colors in the spiral plots were kindly suggested by Daniela Jurado with CONABIO.

## APPENDIX A. PROOFS OF CLAIMS USED IN SECTION 2

**Proof of Proposition 1.** It is immediate that

$$f^{(1)}(t) = -c_1 \left( \frac{2\pi}{L} \right) \sin \left( \frac{2\pi t}{L} - \varphi_1 \right)$$

$$f^{(2)}(t) = -c_1 \left( \frac{2\pi}{L} \right)^2 \cos \left( \frac{2\pi t}{L} - \varphi_1 \right)$$

$$f^{(3)}(t) = - \left( \frac{2\pi}{L} \right)^2 f^{(1)}(t) \tag{12}$$

$$f^{(4)}(t) = - \left( \frac{2\pi}{L} \right)^2 f^{(2)}(t). \tag{13}$$

□

## REFERENCES

- Bai, J. and Ng, S. (2002). Determining the number of factors in approximate factor models. *Econometrica*, 70(1):191–221.
- Baumann, M., Ozdogan, M., Richardson, A. D., and Radeloff, V. C. (2017). Phenology from landsat when data is scarce: Using modis and dynamic time-warping to combine multi-year landsat imagery to derive annual phenology curves. *International Journal of Applied Earth Observation and Geoinformation*, 54:72–83.
- Borgogno-Mondino, E., Lessio, A., and Gomasasca, M. A. (2016). A fast operative method for ndvi uncertainty estimation and its role in vegetation analysis. *European Journal of Remote Sensing*, 49(1):137–156.

- Boschetti, M., Stroppiana, D., Brivio, P., and Bocchi, S. (2009). Multi-year monitoring of rice crop phenology through time series analysis of modis images. *International journal of remote sensing*, 30(18):4643–4662.
- Eastman, M., Ronald, J., and Filk, M. (1993). Long sequence time series evaluation using standardized principal components. *Photogrammetric Engineering and remote sensing*, 59(6):991–996.
- Eklundh, L. and Jönsson, P. (2015). Timesat: A software package for time-series processing and assessment of vegetation dynamics. *Remote sensing time series*, 22:141–158.
- Everitt, B. S., Landau, S., Leese, M., and Stahl, D. (2011). *Cluster Analysis*. Wiley Series in Probability and Statistics. Wiley Online Library.
- Ferraty, F. (2006). *Nonparametric functional data analysis*. Springer.
- Ferraty, F. and Vieu, P. (2006). *Nonparametric Functional Data Analysis*. Springer.
- Filippa, G., Cremonese, E., Migliavacca, M., Galvagno, M., Forkel, M., Wingate, L., Tomelleri, E., Di Cella, U. M., and Richardson, A. D. (2016). Phenopix: A r package for image-based vegetation phenology. *Agricultural and Forest Meteorology*, 220:141–150.
- Heumann, B. W., Seaquist, J., Eklundh, L., and Jönsson, P. (2007). Avhrr derived phenological change in the sahel and soudan, africa, 1982–2005. *Remote sensing of environment*, 108(4):385–392.
- Hopp, R. (1974). *Phenology and seasonality modeling*, chapter Plant phenology observation networks (pp. 25-43. Springer.
- Jakubauskas, M. E., Legates, D. R., Kastens, J. H., et al. (2001). Harmonic analysis of time-series avhrr ndvi data. *Photogrammetric engineering and remote sensing*, 67(4):461–470.
- James, G., Hastie, T., and Sugar, C. (2000). Principal component models for sparse functional data. *Biometrika*, 87:587–602.
- Jönsson, A. M., Eklundh, L., Hellström, M., Barring, L., and Jönsson, P. (2010). Annual changes in modis vegetation indices of swedish coniferous forests in relation to snow dynamics and tree phenology. *Remote Sensing of Environment*, 114(11):2719–2730.
- Jonsson, P. and Eklundh, L. (2002). Seasonality extraction by function fitting to time-series of satellite sensor data. *IEEE transactions on Geoscience and Remote Sensing*, 40(8):1824–1832.
- Klosterman, S. T., Hufkens, K., Gray, J. M., Melaas, E., Sonnentag, O., Lavine, I., Mitchell, L., Norman, R., Friedl, M. A., and Richardson, A. D. (2014). Evaluating remote sensing of deciduous forest phenology at multiple spatial scales using phenocam imagery. *Biogeosciences*, 11(16):4305–4320.
- Kokoszka, P. and Reimherr, M. (2017). *Introduction to functional data analysis*. Chapman and Hall/CRC.
- Kokoszka, P. and Reimherr, M. (2018). *Introduction to Functional Data analysis*. Taylor and Francis.
- Krivobokova, T., Serra, P., Rosales, F., and Klockmann, K. (2022). Joint non-parametric estimation of mean and auto-covariances for gaussian processes. *Computational Statistics & Data Analysis*, 173:107519.
- Liao, C., Wang, J., Dong, T., Shang, J., Liu, J., and Song, Y. (2019). Using spatio-temporal fusion of landsat-8 and modis data to derive phenology, biomass and yield estimates for corn and soybean. *Science of the total environment*, 650:1707–1721.

- Lieth, H. (1974). *Phenology and seasonality modeling*, chapter Purposes of a phenology book (pp. 3-19). Springer.
- López-Pintado, S. and Romo, J. (2009). On the concept of depth for functional data. *Journal of the American statistical Association*, 104(486):718–734.
- Melaas, E. K., Friedl, M. A., and Zhu, Z. (2013). Detecting interannual variation in deciduous broadleaf forest phenology using landsat tm/etm+ data. *Remote Sensing of Environment*, 132:176–185.
- Nietupski, T. C., Kennedy, R. E., Temesgen, H., and Kerns, B. K. (2021). Spatiotemporal image fusion in google earth engine for annual estimates of land surface phenology in a heterogenous landscape. *International Journal of Applied Earth Observation and Geoinformation*, 99:102323.
- Olsson, L. and Eklundh, L. (1994). Fourier series for analysis of temporal sequences of satellite sensor imagery. *International journal of remote sensing*, 15(18):3735–3741.
- Ramsay, J. and Silverman, B. (1997). *Functional Data Analysis*. Springer.
- Ramsay, J. and Silverman, B. (2005). *Functional data analysis*. Springer Series in Statistics. Springer New York, NY, 2nd. edition.
- Reed, B. C., Brown, J. F., VanderZee, D., Loveland, T. R., Merchant, J. W., and Ohlen, D. O. (1994). Measuring phenological variability from satellite imagery. *Journal of vegetation science*, 5(5):703–714.
- Reyes-González, E. R., Gómez-Mendoza, L., Barradas, V. L., and Terán-Cuevas, Á. R. (2021). Cross-scale phenological monitoring in forest ecosystems: a content-analysis-based review. *International Journal of Biometeorology*, 65:2215–2227.
- Roerink, G., Menenti, M., and Verhoef, W. (2000). Reconstructing cloudfree ndvi composites using fourier analysis of time series. *International journal of remote sensing*, 21(9):1911–1917.
- Roy, D. and Yan, L. (2020). Robust landsat-based crop time series modelling. *Remote Sensing of Environment*, 238:110810.
- Ruppert, D., M. W. and Carrol, R. (2003). *Semiparametric Regression*. Cambridge Series in Statistical and Probabilistic Mathematics.
- Sardá-Espinosa, A. (2023). *dtwclust: Time Series Clustering Along with Optimizations for the Dynamic Time Warping Distance*. R package version 5.5.12.
- Sellers, P. J., Tucker, C. J., Collatz, G. J., Los, S., Justice, C., Dazlich, D., and Randall, D. (1994). A global 1 by 1 ndvi data set for climate studies. part 2: The generation of global fields of terrestrial biophysical parameters from the ndvi. *International Journal of remote sensing*, 15(17):3519–3545.
- Sisheber, B., Marshall, M., Mengistu, D., and Nelson, A. (2022). Tracking crop phenology in a highly dynamic landscape with knowledge-based landsat–modis data fusion. *International Journal of Applied Earth Observation and Geoinformation*, 106:102670.
- Sjöström, M., Ardö, J., Arneth, A., Boulain, N., Cappelaere, B., Eklundh, L., De Grandcourt, A., Kutsch, W. L., Merbold, L., Nouvellon, Y., et al. (2011). Exploring the potential of modis evi for modeling gross primary production across african ecosystems. *Remote sensing of environment*, 115(4):1081–1089.
- Tecuapetla-Gómez, I. (2022). *geoTS: Methods for Handling and Analyzing Time Series of Satellite Images*. R package version 0.1.8.

- Tian, T. S. (2010). Functional data analysis in brain imaging studies. *Frontiers in psychology*, 1:1482.
- Yu, Y. (2020). Functional Principal Component Analysis: A Robust Method for Time-Series Phenotypic Data. *Plant Physiology*, 183(4):1422–1423.
- Zeng, L., Wardlow, B. D., Wang, R., Shan, J., Tadesse, T., Hayes, M. J., and Li, D. (2016). A hybrid approach for detecting corn and soybean phenology with time-series modis data. *Remote Sensing of Environment*, 181:237–250.
- Zeng, L., Wardlow, B. D., Xiang, D., Hu, S., and Li, D. (2020). A review of vegetation phenological metrics extraction using time-series, multispectral satellite data. *Remote Sensing of Environment*, 237:111511.
- Zhang, X., Friedl, M. A., Schaaf, C. B., Strahler, A. H., Hodges, J. C., Gao, F., Reed, B. C., and Huete, A. (2003). Monitoring vegetation phenology using modis. *Remote sensing of environment*, 84(3):471–475.
- Zhao, F., Yang, G., Yang, X., Cen, H., Zhu, Y., Han, S., Yang, H., He, Y., and Zhao, C. (2021). Determination of key phenological phases of winter wheat based on the time-weighted dynamic time warping algorithm and modis time-series data. *Remote Sensing*, 13:1836.
- Zheng, Y., Wu, B., Zhang, M., and Zeng, H. (2016). Crop phenology detection using high spatio-temporal resolution data fused from spot5 and modis products. *Sensors*, 16(12):2099.